# Post-Fault Full Torque-Speed Exploitation of Dual Three-Phase IPMSM Drives

Hisham M. Eldeeb, Ayman S. Abdel-Khalik, *Senior Member, IEEE*, Christoph M. Hackl, *Senior Member, IEEE*

***Abstract*—This paper exploits the torque-speed operating limits of a dual three-phase interior permanent magnet synchronous machine (ADT-IPMSM) during post-fault operation for different neutral configurations. To achieve the maximum permissible torque-speed limits, the study proposes software and hardware modifications to the latest fault-tolerant techniques using: (i) an offline optimization that takes into account simultaneously the voltage and current constraints during post-fault operation and (ii) a simple hardware addition that modifies the neutral points configuration to either isolated (1N) or connected (2N) based on the operating torque and/or speed. Compared to literature, the proposed study considers the field-weakening operation, extending the permissible achievable speeds. A 2.5 kW ADT-IPMSM prototype validates the theoretical findings.**

***Index Terms*—Dual three phase, fault-tolerance, IPMSM, post-fault control.**

## NOMENCLATURE

| | |
|---|---|
| *Notation* | |
| $\mathbb{R}$, $\mathbb{N}$ | Set of real and natural numbers |
| $n$, $m \in \mathbb{N}$ | Number of rows and columns |
| $\zeta \in \mathbb{R}$ | Real scalar |
| $\boldsymbol{\zeta} \in \mathbb{R}^n$ | Real vector (bold), expressed as $\boldsymbol{\zeta} = (\zeta_1, \zeta_2, ..., \zeta_n)^\top$ |
| $\|\|\boldsymbol{\zeta}\|\|$ | Euclidean norm of $\boldsymbol{\zeta}$ |
| $\|\|\boldsymbol{\zeta}\|\|_\infty$ | The maximum norm of $\boldsymbol{\zeta}$, i.e. $\|\|\boldsymbol{\zeta}\|\|_\infty = \max\{\|\zeta_1\|, \|\zeta_2\|, ..., \|\zeta_n\|\}$ |
| $\boldsymbol{Z} \in \mathbb{R}^{n\times m}$ | Real $n \times m$ matrix (capital bold) |
| *Subscripts and superscripts* | |
| $\square^\top$ | Transpose operator applied to vector or matrix |
| $\bar{\square}$ | Phasor description of a variable at *steady state* |
| $\square_{\mathrm{s}}$ | Subscript 's' denotes referencing to the stator |
| $\square_{\mathrm{s}}^{\Lambda\lambda}$ | Superscripts '$\Lambda$' and '$\lambda$' are arbitrary variables representing the coordinates of a subspace ($\Lambda \in \{dq, XY, 0^+0^-\}$, $\lambda \in \{dq, XY, 0^+0^-\}$, and $\Lambda \neq \lambda$) |
| *General* | |
| $\boldsymbol{T}_{\mathrm{VSD}} \in \mathbb{R}^{6\times6}$ | Vector space decomposition matrix |
| $\boldsymbol{T}_{\mathrm{p}}(\phi) \in \mathbb{R}^{2\times2}$ | Park's transformation with angle $\phi \in \mathbb{R}$ |
| $\boldsymbol{T}_k \in \mathbb{R}^{6\times2}$ | Optimization matrix |
| $k_\Gamma^\alpha$, $k_\Gamma^\beta$ | Scalar optimization parameters in $\boldsymbol{T}_k$ of the $\Gamma \in \{X, Y\}$ coordinate |
| $\boldsymbol{J} \in \mathbb{R}^{2\times2}$ | Rotation matrix |
| $u$ | Electrical voltage (V) |
| $i$ | Electrical current (A) |
| $\psi$ | Flux linkage (Wb) |
| $\boldsymbol{\zeta}_{\mathrm{s}}^{a_1\to c_2} \in \mathbb{R}^6$ | Stator space vector expressed in the $(\mathrm{a_1b_1c_1\text{-}a_2b_2c_2})$ frame, where $\boldsymbol{\zeta} \in \{\boldsymbol{u}, \boldsymbol{\psi}, \boldsymbol{i}\}$) |
| $u_{\mathrm{dc}}$ | DC-link voltage (V) |
| $m_{\mathrm{e}}$ | Electromechanical torque (N·m) |
| $m_{\mathrm{e,max}}$ | Maximum torque for a given neutral point configuration (N·m) |
| $m_{\mathrm{load}}$ | Load torque (N·m) |
| $n_{\mathrm{p}}$ | Pole-pair number |
| $\omega_{\mathrm{e}}$ | Electrical angular speed (rad/s) |
| $\Omega_{\mathrm{e}}^{\mathrm{MTPA}}$ | Speed trajectories per every permissible $m_{\mathrm{e}}$ of the MTPA criteria (rad/s) |
| $\Omega_{\mathrm{e}}^{\mathrm{FW}}$ | Speed trajectories per every permissible $m_{\mathrm{e}}$ of the FW criteria (rad/s) |
| $\omega_{\mathrm{e,max}}^{\mathrm{FW}}$ | Maximum speed within the $\Omega_{\mathrm{e}}^{\mathrm{FW}}$ loci (rad/s) |
| $\phi_{\mathrm{e}}$ | Electrical angular position referred to reference flux axis of phase $a_1$ (rad) |
| $\nu$ | Viscous friction coefficient (N·m·s) |
| $m_{\mathrm{c}}$ | Coulomb friction torque (N·m) |
| $m_{\mathrm{fric}}$ | Total friction torque (N·m) |
| $\Theta$ | Mechanical inertia (kg·m$^2$) |
| $R_{\mathrm{s}}$ | Stator electrical resistance ($\Omega$) |
| $\boldsymbol{L}_{\mathrm{s}}^{\Lambda\lambda} \in \mathbb{R}^{2\times2}$ | Inductance matrix of the $\Lambda\lambda$ subspace (H) |
| $L_{\mathrm{s}}^d$, $L_{\mathrm{s}}^q$ | Inductance of the $d$- and $q$-axis (H) |
| $L_m^{dq}$ | Cross-coupling inductance of the $dq$ subspace (H) |

Manuscript received April 27, 2018; revised June 22, 2018; September 04, 2018; accepted October 26, 2018.

Hisham M. Eldeeb is with Munich University of Applied Sciences (MUAS) and Munich School of Engineering, Technical University of Munich (TUM), in the research group: Control of Renewable Energy Systems (CRES) (e-mail: hisham.eldeeb@tum.de).

A. S. Abdel-Khalik is with Electrical Engineering Department, Faculty of Engineering, Alexandria University, Alexandria 21544, Egypt (e-mail: ayman.abdel-khalik@alexu.edu.eg).

Christoph M. Hackl is with MUAS and head of the CRES research group at TUM (e-mail: christoph.hackl@hm.edu).

## I. INTRODUCTION

COMPARED to the standard three-phase industrial drives, multi-phase drives are an attractive alternative owing to their inherent fault-tolerance capability, enhanced efficiency, and rating reduction of the employed voltage-source inverter (VSI) [1]–[3]. Such drives are common for high-reliability-demanding applications as ship propulsion, avionics and electric vehicles (EV); where prolonged operation in the presence of faults is expected [1], [3], [4]. Accordingly, fault-tolerant research studies of different types of multi-phase drives received significant attention in the last decade [4]–[7], especially those faults related to the VSIs, being the most common sources of faults [8]. Assuming that the fault is detected and cleared, several post-fault control strategies have been proposed for

one or more open-phase faults (OPFs) [4], [6]. For machines with distributed windings, if the number of phases is divisible by three, then the multi-phase machine can be obtained out of a former three-phase machine [9]. Thus, six-phase, also known as dual three-phase machines (DTMs), are one of the promising topologies of multi-phase drives. In that case, a spatial phase shift of $\pi/3$ or $\pi/6$ between the two three phase windings lead to symmetrical or asymmetrical configuration, respectively, where the latter is the type discussed in this paper.

In the pre-fault case (i.e. healthy case), the non-fundamental subspace currents are regulated to zero to ensure balanced currents and high-performance operation [10]. On the other hand, in the post-fault operation, fundamental currents are forced into the non-fundamental subspaces; with an aim to keep the same magneto-motive force in the air-gap [5], [7], [8]. The amplitudes and phase shifts of such forced currents are determined based on the neutral point configuration (i.e. isolated (1N) or connected (2N)) and, accordingly, the carried-out post fault optimization. Given that the objective during post-fault operation is to generate the desired uninterrupted electromagnetic torque, such optimization is divided in literature into three types: minimum Joule losses (ML), maximum torque (MT), and a *hybrid* minimum losses maximum torque (MLMT) [5], [7]. The main difference between such optimization techniques lies in the defined optimization constraints, which affect how the amplitudes and phase shifts of the forced fundamental currents are scaled in the different subspace coordinates. The ML optimization constraints minimize the total stator Joule losses for a given reference torque, leading to limited torque-production capability and unequal loading of different phases [11]. MT maximizes the electromagnetic torque through maximizing the stator currents up to the rated current value. This results in equal loading for the healthy phases at the expense of higher total copper losses, when compared with ML [5]. It was proved in [7] that the hybrid MLMT optimization is capable of combining the merits of ML and MT, such that minimum losses is ensured for every permissible torque reference.

To the best of the authors' knowledge, the available publications focused on optimising the production of the desired torque, under the following assumptions:

- The neutral configuration 1N is the preferred neutral point configuration from fault tolerance point of view [5], [7];
- The DC-link voltage reserve is not taken into account in the optimization algorithm. This implies that the rated stator voltage would not be violated and the machine can be driven at the same speeds as in the healthy case. This assumption is unachievable and critical as for some applications, operating the drive in the overspeed region (i.e. field-weakening (FW)) is inevitable as in EV [12];

Given the aforementioned limitations and assumptions, this paper takes into account the stator voltage as a constraint within the optimization algorithm, which in turn affects the operational speeds of the drive, as seen in the recent study in [13] which focused only on three-phase induction machines. A comparison between the torque-speed characteristics of 1N and 2N configurations is carried-out. It will be shown that

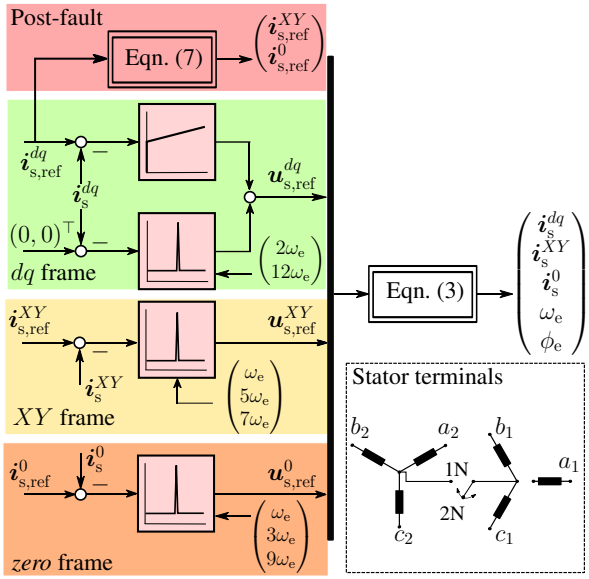


Fig. 1. Post-fault fundamental and harmonic current controllers with the corresponding resonant frequencies [10], [14].

TABLE I. Parameters of the ADT-IPMSM drive.

| Parameter | Value |
|---|---|
| Stator resistance | $R_\mathrm{s} = 1.1\,\Omega$ |
| $X$-axis leakage inductance* | $L_\mathrm{s}^X = 2.42$ mH |
| $Y$-axis leakage inductance* | $L_\mathrm{s}^Y = 2.04$ mH |
| $0^+$-axis inductance* | $L_\mathrm{s}^{0^+} = 2.7$ mH |
| $0^-$-axis inductance* | $L_\mathrm{s}^{0^-} = 2.61$ mH |
| Pole-pair | $n_\mathrm{p} = 3$ |
| Inertia | $\Theta = 0.01$ kg·m$^2$ |
| Viscous friction coefficient | $\nu = 0.8 \times 10^{-3}$ N·m·s |
| Coulomb friction | $m_\mathrm{c} = 0.2725$ N·m |
| Rated stator peak current | $\hat{i}_\mathrm{s,rated} = 4.1\sqrt{2}$ A |
| Rated stator peak voltage | $\hat{u}_\mathrm{s,rated}^{l\text{-}l} = 170\sqrt{2}$ V |
| Rated torque | $m_\mathrm{e,rated} = 10.6$ N·m |
| Rated mechanical speed | 2300 RPM |
| Sampling and switching frequencies | $f_\mathrm{sw} = 8$ kHz |

* Average of the corresponding inductances in [14].

the 2N connection is capable of extending the overspeed region compared to the 1N connection, which was favoured previously in literature in terms of torque production [6]. Furthermore, a hybrid neutral point connection is proposed to combine the merits of both 1N and 2N connections based on the torque-speed operating point. The effect of the PM harmonics as well as the discrete time delay are taken into account within the employed current controller; to ensure high-performance stable operation within the entire permissible speed range. The concluded results for one OPF can be extrapolated to various multi-phase machines and for other OPFs. The optimization algorithm has been validated on a 2.5 kW ADT-IPMSM setup.

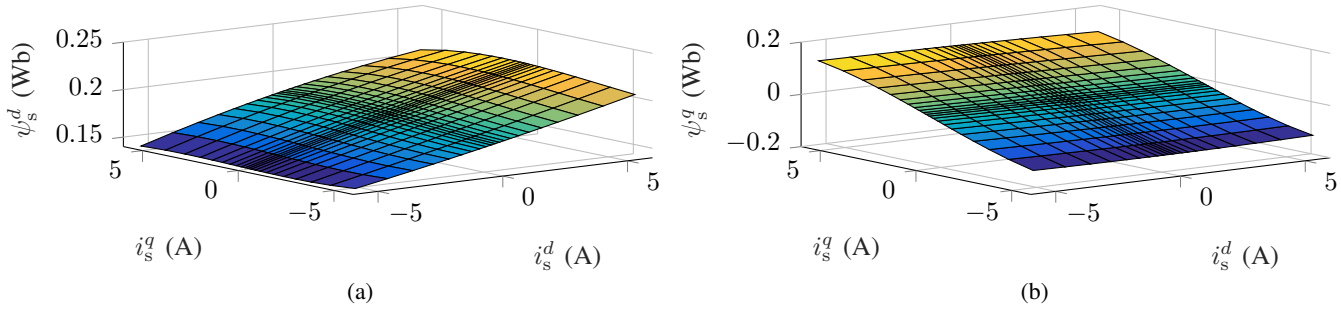


(a) (b)

Fig. 2. Measured flux linkage maps of $\boldsymbol{\psi}_s^{dq}$ in (3), showing the variation of (a) $\psi_s^d$ and (b) $\psi_s^q$ for $||\boldsymbol{i}_s^{dq}|| \leq \hat{i}_{s,\text{rated}}$.

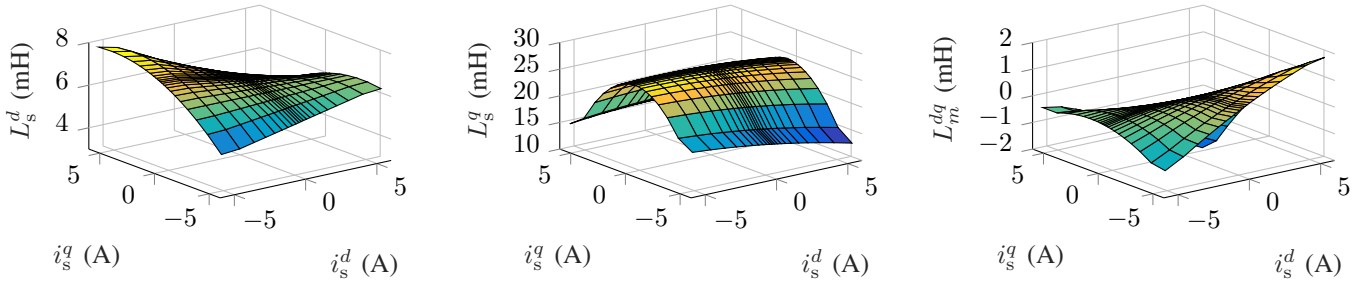


(a) (b) (c)

Fig. 3. Measured differential inductances of (a) $L_s^d$ (b) $L_s^q$ (c) $L_m^{dq}$ within the domain $||\boldsymbol{i}_s^{dq}|| \leq \hat{i}_{s,\text{rated}}$.

## II. Asymmetrical Dual Three Phase IPMSM Model

Similar to the Clarke's transformation for three-phase drives, the vector space decomposition (VSD) transformation [6],

$$\boldsymbol{T}_{\text{VSD}} = \frac{1}{3}\begin{bmatrix} 1 & -\frac{1}{2} & -\frac{1}{2} & \frac{\sqrt{3}}{2} & -\frac{\sqrt{3}}{2} & 0 \\ 0 & \frac{\sqrt{3}}{2} & -\frac{\sqrt{3}}{2} & \frac{1}{2} & \frac{1}{2} & -1 \\ 1 & -\frac{1}{2} & -\frac{1}{2} & -\frac{\sqrt{3}}{2} & \frac{\sqrt{3}}{2} & 0 \\ 0 & -\frac{\sqrt{3}}{2} & \frac{\sqrt{3}}{2} & \frac{1}{2} & \frac{1}{2} & -1 \\ 1 & 1 & 1 & 0 & 0 & 0 \\ 0 & 0 & 0 & 1 & 1 & 1 \end{bmatrix}, \tag{1}$$

decomposes the $a_1b_1c_1$-$a_2b_2c_2$ asymmetrical six-phase quantities $\boldsymbol{f}_s^{a_1\to c_2}$, where $f \in \{u, \psi, i\}$, on three orthogonal planes $\left(\boldsymbol{f}_s^{\alpha\beta}, \quad \boldsymbol{f}_s^{XY}, \quad \boldsymbol{f}_s^{0}\right)^\top = \boldsymbol{f}_{s,\text{VSD}} = \boldsymbol{T}_{\text{VSD}}\boldsymbol{f}_s^{a_1\to c_2}$, namely the equivalent $\alpha\beta$ subspace, "0" subspace representing the *zero* sequence components from both three-phase sets (i.e. $\boldsymbol{f}_s^0 = (f_s^{0+}, f_s^{0-})^\top$), and the $XY$ subspace, which relates to the degree of unbalance between the two three-phase sets [4], [6], [8], [14]. Moreover, different harmonics are mapped to such subspaces, where $\alpha\beta$ plane holds the $12\gamma \pm 1$ harmonics, where $\gamma = \{1, 2, 3, ...\}$, $XY$ is concerned with the $6\delta \pm 1$ harmonics, where $\delta = \{1, 3, 5, ...\}$, and $0^+0^-$ is responsible for the triplets harmonics $3\delta$. Applying Park's transformation

$$\boldsymbol{T}_{\text{p}}(\phi_{\text{e}})^{-1} \quad = \quad \begin{bmatrix} \cos(\phi_{\text{e}}) & -\sin(\phi_{\text{e}}) \\ \sin(\phi_{\text{e}}) & \cos(\phi_{\text{e}}) \end{bmatrix}, \tag{2}$$

to the $f_s^{\alpha\beta}$ quantities, the ADTM-IPMSM dynamic model can be written in a compact vector form as

$$\left.\begin{aligned} \boldsymbol{u}_s^{dq} &= R_s\,\boldsymbol{i}_s^{dq} + \omega_e\,\boldsymbol{J}\boldsymbol{\psi}_s^{dq} + \tfrac{\text{d}}{\text{d}t}\boldsymbol{\psi}_s^{dq}, \\ \boldsymbol{u}_s^{XY} &= R_s\,\boldsymbol{i}_s^{XY} + \boldsymbol{L}_s^{XY}\tfrac{\text{d}}{\text{d}t}\boldsymbol{i}_s^{XY} + \tfrac{\text{d}}{\text{d}t}\boldsymbol{\psi}_s^{XY}, \\ \boldsymbol{u}_s^{0} &= R_s\,\boldsymbol{i}_s^{0} + \boldsymbol{L}_s^{0}\tfrac{\text{d}}{\text{d}t}\boldsymbol{i}_s^{0} + \tfrac{\text{d}}{\text{d}t}\boldsymbol{\psi}_s^{0}, \\ \tfrac{\Theta}{n_p}\tfrac{\text{d}\omega_e}{\text{d}t} &= \underbrace{3\,n_p\boldsymbol{i}_s^{dq\top}\,\boldsymbol{J}\,\boldsymbol{\psi}_s^{dq}}_{=m_e} - m_{\text{load}} - m_{\text{fric}}, \end{aligned}\right\} \tag{3}$$

where $\boldsymbol{J} := \boldsymbol{T}_{\text{p}}(\frac{\pi}{2})^{-1}$, $\boldsymbol{L}_s^{XY} = \text{diag}(L_s^X, L_s^Y)$, $\boldsymbol{L}_s^0 = \text{diag}(L_s^{0^+}, L_s^{0^-})$ and $m_{\text{fric}} = \nu\frac{\omega_e}{n_p} + m_c$. The ADT-IPMSM parameters are shown in Table I. $\boldsymbol{\psi}_s^{dq}$ models the fundamental flux linkage, while $\boldsymbol{\psi}_s^{XY}$ and $\boldsymbol{\psi}_s^0$ represent the harmonic flux linkages as excerpted from [14]. The post-fault control structure is depicted in Fig. 1. The model considers non-linear flux linkages variations of $\boldsymbol{\psi}_s^{dq}$, leading to differential $dq$-axes inductances $L_s^d$, $L_s^q$ and the cross-coupling inductance $L_m^{dq}$, which are dependent on $\boldsymbol{i}_s^{dq}$ (see Figs. 2 and 3) [15, Chapter 14]. This improves not only the modelling from simulations point of view, but also enhances the current controller and dynamical modelling [14], [16]. Even if such non-linearity is neglected (i.e. assuming linear flux linkages), the philosophy of the proposed optimization, shown later in Sect. III, would still hold. The upcoming discussion assumes the knowledge of the faulty phase(s). The reader is referred to [17] for studying the transition from the healthy to the post-fault operation and the detection of the faulty phase(s), which is not exploited in this paper.

## III. Post-Fault Torque-Speed Exploitation

### A. Post-fault subspace and phase currents

As proved in [5], the fundamental subspace (i.e. $dq$ and $\alpha\beta$) in the post-fault operation is still the one responsible for the torque production, where in this case $m_e$ still depends on relation with the fundamental currents (i.e. $m_e$ in (3) holds). The upcoming analysis lays its foundation on the presented post-fault analysis and the equations introduced in [5], [7], [18], where the optimization relied on injecting fundamental currents in the $XY$ subspace for the 2N connection and in both the $XY$ and $0^+0^-$ subspaces for the 1N connection. Accordingly, in the post-fault operation, assuming a fault in

phase $\mathrm{a}_1$, then $\bar{\boldsymbol{i}}_{\mathrm{s,VSD}}$ can be related to $\bar{\boldsymbol{i}}_{\mathrm{s}}^{\alpha\beta}$ at *steady state* as [7], [18]

$$\bar{\boldsymbol{i}}_{\mathrm{s,VSD}} = \underbrace{\begin{bmatrix} 1 & 0 \\ 0 & 1 \\ k_X^{\alpha} & k_X^{\beta} \\ k_Y^{\alpha} & k_Y^{\beta} \\ -1-k_X^{\alpha} & -k_X^{\beta} \\ 1+k_X^{\alpha} & k_X^{\beta} \end{bmatrix}}_{=:\boldsymbol{T}_k \,\in\, \mathbb{R}^{6\times 2}} \bar{\boldsymbol{i}}_{\mathrm{s}}^{\alpha\beta}, \tag{4}$$

where the accent "$\bar{\square}$" is the phasor description of a variable at *steady state*. $\boldsymbol{T}_k$ is the optimization matrix, varied to fulfill the necessary constraints (introduced later in Sect. III-C). The parameters $k_X^{\alpha}$, $k_X^{\beta}$, $k_Y^{\alpha}$, and $k_Y^{\beta}$ are scalar parameters resulting from running the optimizer *fmincon* in Matlab upon passing the cost function and the constraints as seen shortly in Sect. III-C. For the 2N connection, the path for zero sequence currents is blocked (i.e. open circuit). Thus, $i_{\mathrm{s}}^{0^+} = i_{\mathrm{s}}^{0^-} = 0$, which when substituting in (4) leads to $k_X^{\alpha} = -1$, $k_X^{\beta} = 0$. For either neutral connection, the phase currents can be expressed as [5], [7]

$$\bar{\boldsymbol{i}}_{\mathrm{s}}^{a_1\rightarrow c_2} = \boldsymbol{T}_{\mathrm{VSD}}^{-1}\,\boldsymbol{T}_k\,\bar{\boldsymbol{i}}_{\mathrm{s}}^{\alpha\beta}. \tag{5}$$

### B. Post-fault voltages

The post-fault analysis studies at steady state the effect of injecting of fundamental currents in the non-torque-producing subspaces. Thus, the study of the voltage evolution in the different subspaces deals only with the fundamental component. Although the flux linkages model in (3) is a function of the PM harmonic components [14], such harmonics will be dealt with during the implementation of the stator current controller (see Fig. 1), as seen later in Sect. IV. Thus, for a given $m_{\mathrm{e}}$ and $\omega_{\mathrm{e}}$, the post-fault fundamental *steady state* model for the different subspaces can be deduced from (3) as

$$\left.\begin{aligned} \boldsymbol{u}_{\mathrm{s}}^{dq} &= R_{\mathrm{s}}\,\boldsymbol{i}_{\mathrm{s}}^{dq} + \omega_{\mathrm{e}}\,\boldsymbol{J}\boldsymbol{\psi}_{\mathrm{s}}^{dq}, \\ \bar{\boldsymbol{u}}_{\mathrm{s}}^{XY} &= R_{\mathrm{s}}\,\bar{\boldsymbol{i}}_{\mathrm{s}}^{XY} + \omega_{\mathrm{e}}\boldsymbol{J}\boldsymbol{L}_{\mathrm{s}}^{XY}\,\bar{\boldsymbol{i}}_{\mathrm{s}}^{XY}, \\ \bar{\boldsymbol{u}}_{\mathrm{s}}^{0} &= R_{\mathrm{s}}\,\bar{\boldsymbol{i}}_{\mathrm{s}}^{0} + \omega_{\mathrm{e}}\boldsymbol{J}\boldsymbol{L}_{\mathrm{s}}^{0}\,\bar{\boldsymbol{i}}_{\mathrm{s}}^{0}. \end{aligned}\right\} \tag{6}$$

Using the phasor representation of the $\alpha\beta$ in terms of the $dq$ variables (i.e. derived from (2)) and the relation between the different subspaces in (4), one can rewrite (4) in polar coordinates as

$$\bar{\boldsymbol{i}}_{\mathrm{s,VSD}} \overset{(2),(4)}{=} ||\boldsymbol{i}_{\mathrm{s}}^{dq}|| \begin{pmatrix} \angle\phi_{dq} \\ \angle\phi_{dq} - \frac{\pi}{2} \\ |k_X^{\alpha\beta}|\angle\phi_{dq} - \phi_x \\ |k_Y^{\alpha\beta}|\angle\phi_{dq} - \phi_y - \frac{\pi}{2} \\ |k_{0^+}^{\alpha\beta}|\angle\phi_{dq} - \phi_0 \\ |k_{0^+}^{\alpha\beta}|\angle\phi_{dq} - \phi_0 - \pi \end{pmatrix}. \tag{7}$$

The mathematical manipulations are omitted for space limitations and hold under the following definitions $\phi_{dq} = \tan^{-1}(i_{\mathrm{s}}^{q}/i_{\mathrm{s}}^{d})$; $\phi_x := \tan^{-1}(k_X^{\beta}/k_X^{\alpha})$; $\phi_y := \tan^{-1}(k_Y^{\alpha}/k_Y^{\alpha})$; $\phi_0 := \tan^{-1}\big(k_X^{\beta}/(1+k_X^{\alpha})\big)$; $|k_X^{\alpha\beta}| := \sqrt{(k_X^{\alpha})^2 + (k_X^{\beta})^2}$; $|k_Y^{\alpha\beta}| := \sqrt{(k_Y^{\alpha})^2 + (k_Y^{\beta})^2}$; $|k_{0^+}^{\alpha\beta}| := \sqrt{(1+k_X^{\alpha})^2 + (k_X^{\beta})^2}$. Upon computing the subspace voltages in (6) and the phasor voltage in the $\alpha\beta$ subspace $\bar{\boldsymbol{u}}_{\mathrm{s}}^{\alpha\beta}$ out of $\boldsymbol{u}_{\mathrm{s}}^{dq}$, it is possible to compute the corresponding stator phase voltages by applying the inverse of the VSD matrix in (1) leading to

$$\bar{\boldsymbol{u}}_{\mathrm{s}}^{a_1\rightarrow c_2} = \boldsymbol{T}_{\mathrm{VSD}}^{-1}\,\bar{\boldsymbol{u}}_{\mathrm{s,VSD}}. \tag{8}$$

It is necessary to mention that the unbalance that took place with one or more OPFs may require the application of unbalanced voltages in order to sustain the desired magneto-motive force and, hence, the developed electromagnetic torque. Accordingly, it is essential to ensure that the line-to-line stator voltages of the healthy phases $\bar{\boldsymbol{u}}_{\mathrm{s,2N}}^{l\text{-}l}$ for the 2N case

$$\bar{\boldsymbol{u}}_{\mathrm{s,2N}}^{l\text{-}l} = \underbrace{\begin{bmatrix} 0 & 1 & -1 & 0 & 0 & 0 \\ 0 & 0 & 0 & 1 & -1 & 0 \\ 0 & 0 & 0 & 0 & 1 & -1 \\ 0 & 0 & 0 & -1 & 0 & 1 \end{bmatrix}}_{=:\boldsymbol{T}_{\mathrm{2N}}^{l\text{-}l} \,\in\, \mathbb{R}^{4\times 6}} \bar{\boldsymbol{u}}_{\mathrm{s}}^{a_1\rightarrow c_2}, \tag{9}$$

and $\bar{\boldsymbol{u}}_{\mathrm{s,1N}}^{l\text{-}l}$ for the 1N case

$$\bar{\boldsymbol{u}}_{\mathrm{s,1N}}^{l\text{-}l} = \underbrace{\begin{bmatrix} 0 & 1 & -1 & 0 & 0 & 0 \\ 0 & 1 & 0 & -1 & 0 & 0 \\ 0 & 1 & 0 & 0 & -1 & 0 \\ 0 & 1 & 0 & 0 & 0 & -1 \\ 0 & 0 & 1 & -1 & 0 & 0 \\ 0 & 0 & 1 & 0 & -1 & 0 \\ 0 & 0 & 1 & 0 & 0 & -1 \\ 0 & 0 & 0 & 1 & -1 & 0 \\ 0 & 0 & 0 & 0 & 1 & -1 \\ 0 & 0 & 0 & -1 & 0 & 1 \end{bmatrix}}_{=:\boldsymbol{T}_{\mathrm{1N}}^{l\text{-}l} \,\in\, \mathbb{R}^{10\times 6}} \bar{\boldsymbol{u}}_{\mathrm{s}}^{a_1\rightarrow c_2}, \tag{10}$$

would not exceed the rated peak value $\hat{u}_{\mathrm{s,rated}}^{l\text{-}l}$, which determines the required $u_{\mathrm{dc}}$. In (9), the line-to-line voltages in $\bar{\boldsymbol{u}}_{\mathrm{s,2N}}^{l\text{-}l}$ consider the voltages of the two three-phase sets separately; since the neutral points are isolated. As for (10), all possible voltage combinations, excluding the faulty phase(s) should be considered, owing to the unbalanced voltages in the post-fault operation. Taking such voltages $\bar{\boldsymbol{u}}_{\mathrm{s,1N}}^{l\text{-}l}$ and $\bar{\boldsymbol{u}}_{\mathrm{s,2N}}^{l\text{-}l}$ into account ensures also that the dual three-phase inverter will not be driven into the over-modulation region [9].

### C. Post-fault optimization

Given the modelled post-fault currents and voltages for both 1N and 2N connections in Sects. III-A and III-B, defining the sets of phases as $\mathbb{S} \in \{\mathrm{a}_1, \ldots, \mathrm{c}_2\}$, faulty phases $h_f$ and the healthy phases $h := \mathbb{S} \setminus h_f$ (i.e. $h \cap h_f = \varnothing$); the generalized objective function can be formulated at a given speed as

$$\min_{\boldsymbol{T}_k}\ p_{\mathrm{Cu}} = \frac{(\boldsymbol{i}_{\mathrm{s}}^{h})^{\top}\,\boldsymbol{i}_{\mathrm{s}}^{h}}{6(i_{\mathrm{s,rated}})^2}, \tag{11}$$

subject to the following constraints:

$$\left.\begin{aligned} g_1:&\quad i_{\mathrm{s}}^{h_f} = 0, \\ g_2:&\quad \sum_{\gamma\in h} i_{\mathrm{s}}^{\gamma} = 0, \\ g_3:&\quad m_{\mathrm{e}} = m_{\mathrm{e,ref}}, \\ g_4:&\quad ||\boldsymbol{i}_{\mathrm{s}}^{h}||_{\infty} \le \hat{i}_{\mathrm{s,rated}}, \\ g_5:&\quad \begin{cases} ||\bar{\boldsymbol{u}}_{\mathrm{s,1N}}^{l\text{-}l}||_{\infty} \le \hat{u}_{\mathrm{s,rated}}^{l\text{-}l}, & \text{1N case}, \\ ||\bar{\boldsymbol{u}}_{\mathrm{s,2N}}^{l\text{-}l}||_{\infty} \le \hat{u}_{\mathrm{s,rated}}^{l\text{-}l}, & \text{2N case}, \end{cases} \end{aligned}\right\} \tag{12}$$

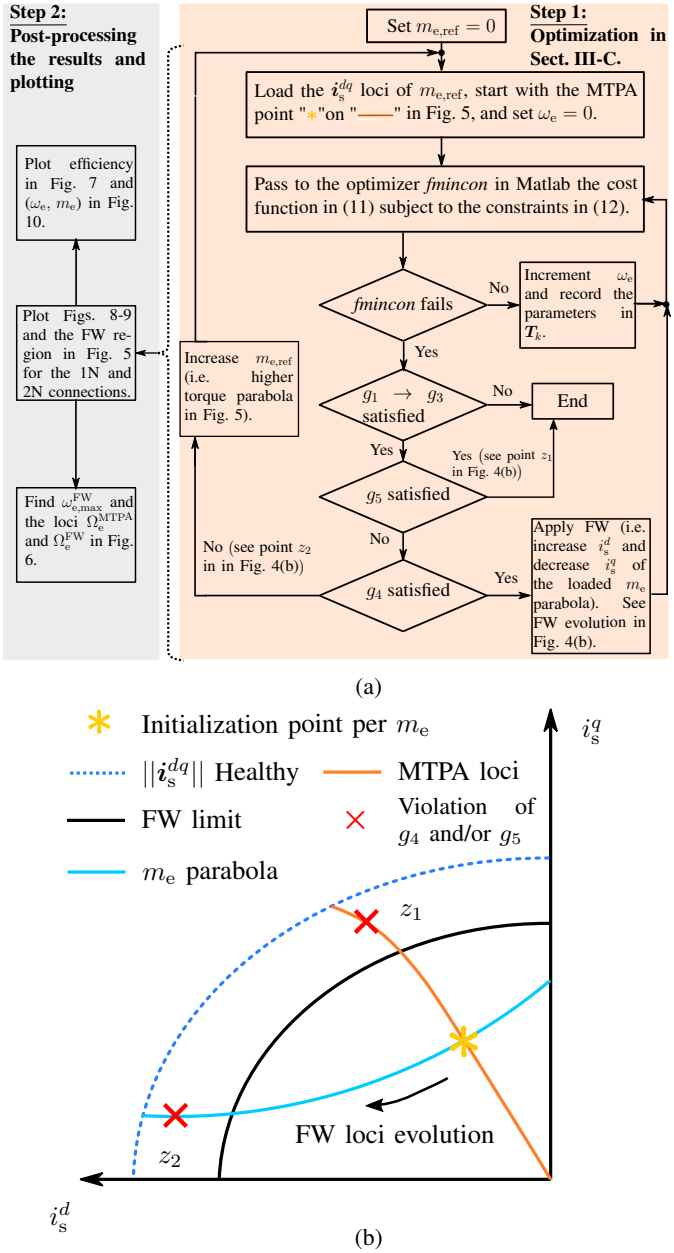


Fig. 4. (a) Post-fault flowchart of the proposed optimization in Sect. III-C applied for the 1N and 2N configurations along with (b) an exemplary representation showing the evolution of $i_s^{dq}$ points for a loaded $m_e$ parabola. Points similar to $z_1$ (i.e. on the MTPA loci and beyond the FW limit) violate $g_5$ in (12), while points similar to $z_2$ (i.e. on the FW loci and beyond the FW limit) violate $g_4$ and $g_5$.

where $p_{Cu}$ is the normalized stator copper losses with respect to the healthy case. Note that the constraints $g_1 \rightarrow g_4$ in (12) were already covered in [7], while the constraint $g_5$ has been introduced to take into account the effect of the limited voltage reserve, especially when the machine is driven into the FW region. Although the upcoming optimization is carried-out for one OPF (i.e. phase $a_1$), the presented methodology can be extrapolated to cover the remaining unique OPFs shown in [6]. Considering $g_5$, unlike in [7], [18], will achieve in the post-fault operation limited speeds per every permissible torque, termed $\Omega_e^{MTPA}$, which defines the loci of the maximum speeds corresponding to the Maximum-Torque-per-Ampere (MTPA) criteria. The maximum field-weakening (FW) speed trajectories for every torque is termed $\Omega_e^{FW}$, while the maximum achievable speed within $\Omega_e^{FW}$ is $\omega_{e,max}^{FW}$, which is the maximum FW speed at no-load. The optimization begins by setting the reference torque $m_{e,ref} = 0$ and loading the corresponding $i_s^{dq}$ loci for such torque. The algorithm is initialized with $i_s^{dq}$ at the MTPA point. Starting from standstill, $\omega_e$ is varied while ensuring the constraints in (12) are satisfied and recording the parameters in $T_k$. Moreover, the remaining $i_s^{dq}$ points are swept and the corresponding parameters in $T_k$ are stored. Afterwards, the reference torque is increased while repeating the similar process, as previously explained, till reaching the point that the initializing MTPA point does not satisfy $g_4$. The proposed optimization is summarized in the flowchart shown in Fig. 4(a) with the aid of Fig. 4(b). In Fig. 4(a), the decision block for $g_1 \rightarrow g_3$ is to ensure that the constraints of the physical system $g_1$ and $g_2$ are not violated, as well as the produced torque matches $m_{e,ref}$ (i.e. $g_3$), when searching for a feasible $T_k$. By running the optimization function *fmincon* in Matlab, it was concluded that failure to find a feasible $T_k$ per every iteration would result from violating $g_4$ and/or $g_5$. The post-processing of the optimization involves plotting Figs. 5-9 for 1N and 2N, extraction of the $\Omega_e^{MTPA}$ and $\Omega_e^{FW}$ loci, and the maximal speed limit $\omega_{e,max}^{FW}$. The outcomes of such optimization, represented in Figs. 5-9, are detailed in the next Section. It is worth to mention that even though the effect of saturation was taken into account in the proposed optimization in (12), by invoking the non-linear $\psi_s^{dq}$ in (6) (see Figs. 2 and 3), the effect of varying $R_s$ (i.e. due to aging or overheating) would not lead to different outcomes than those presented shortly in the next section. This is due to the fact that practical multi-phase machines address high power applications with negligible stator resistance compared with the machine stator impedance.

### D. Torque-speed characteristics

Upon completing the proposed optimization in Sect.III-C, the relation between the permissible torques, speeds, currents and the corresponding parameters in $T_k$ can be graphically represented as shown in Figs. 5-9, respectively. Figs. 5(a)-(b) highlight in ■ the post-fault FW permissible region of the 1N and 2N connections, respectively. The current loci indicated by "*" represent the corresponding loci when applying the algorithm in [7]. The derating is clear with respect to the pre-fault (i.e. healthy) case.

The fact that the 1N connection covers a larger operating area within the $dq$ current loci in Fig. 5(a), in comparison with the 2N connection in Fig. 5(b), adheres to the drawn conclusions in [5]–[7]. Defining $m_{e,max}$ as the maximum torque for a given neutral point configuration, the torque per ampere capability of the 1N is superior with a recorded $m_{e,max}$ 22% higher torque production than that of the 2N connection.

On the other hand, the achievable maximum speeds (i.e. $\Omega_e^{MTPA}$ and $\Omega_e^{FW}$) in Fig. 6(a) are inferior to the 2N case as illustrated in Fig. 6(b). This is due to the fact that the available voltage reserve is distributed among the $dq$ and $XY$ subspaces in the 2N connection, compared to the 1N case,

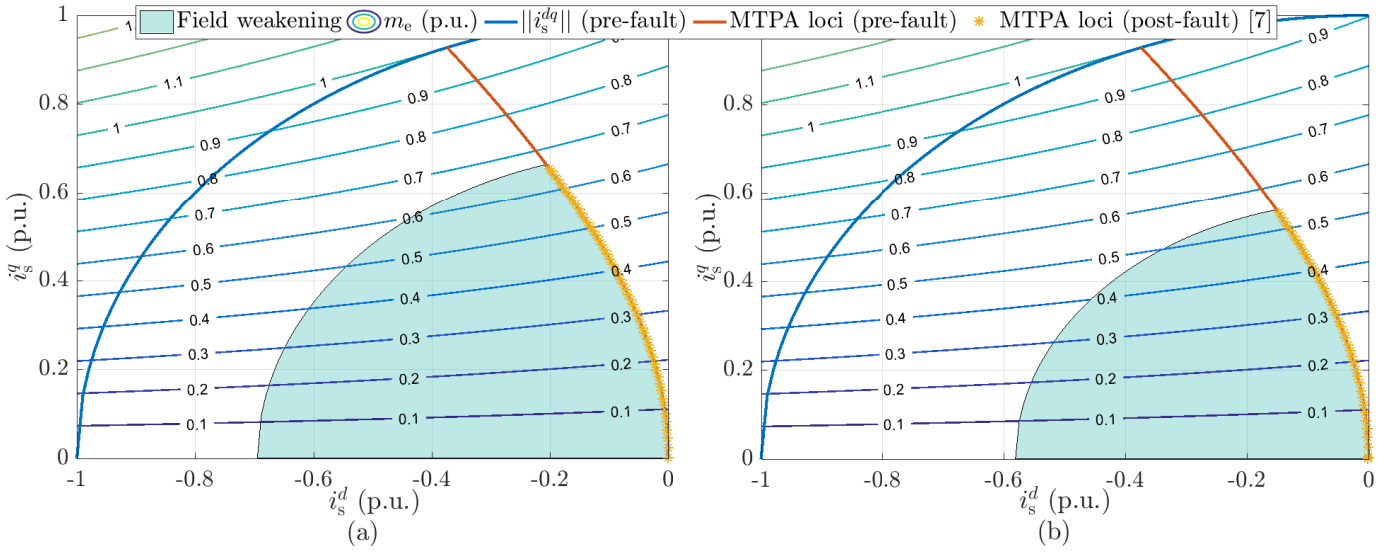


Fig. 5. Post-fault $i_s^{dq}$ loci comparison between the presented post-fault algorithm in [7] and proposed optimization in Sect. III-C, which covers additionally the FW region of (a) 1N and (b) 2N neutral configurations.

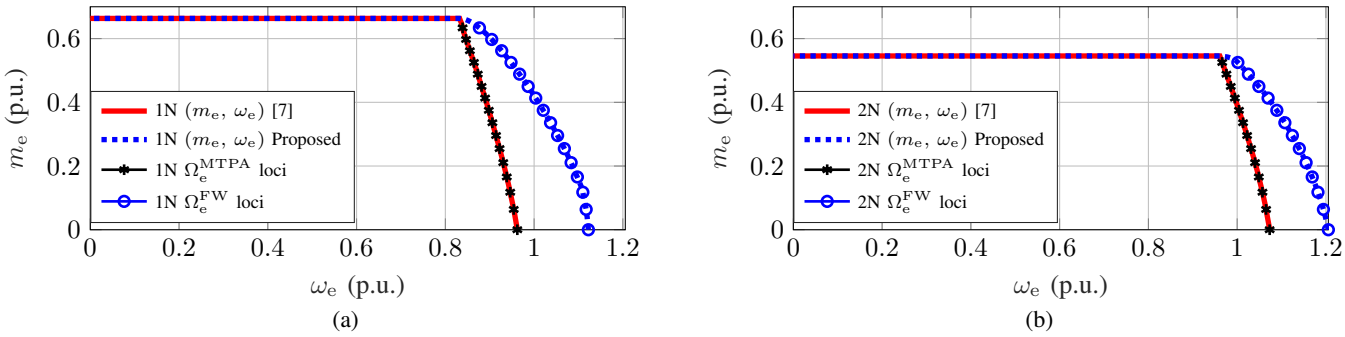


Fig. 6. Post-fault comparison of the permissible ($m_e$, $\omega_e$) characteristics between the presented algorithm in [7] and proposed optimization in Sect. III-C with respect to the (a) 1N and (b) 2N neutral configurations, showing the enhancement in terms of extending the permissible speed ranges.

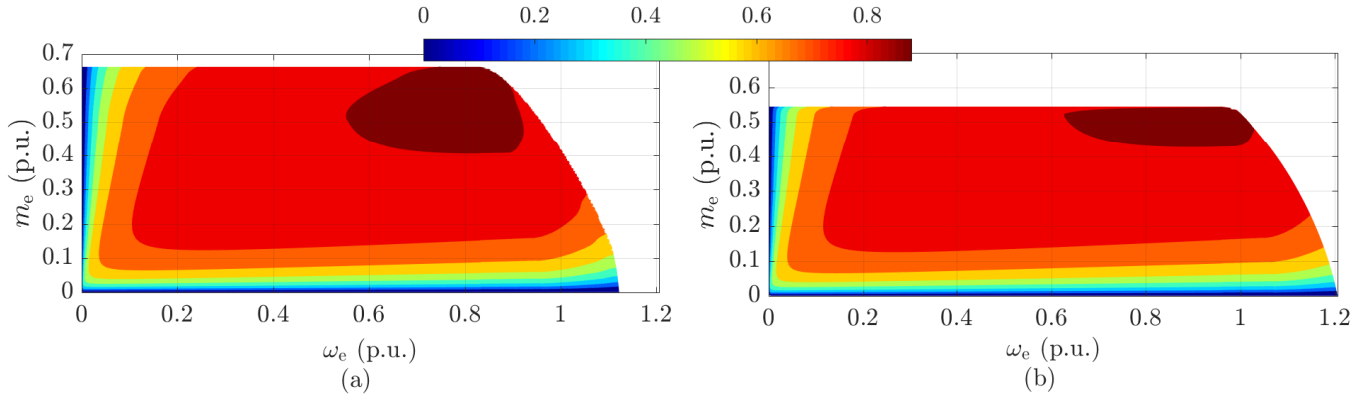


Fig. 7. Post-fault efficiency maps of (a) 1N and (b) 2N connections within the ($m_e$, $\omega_e$) range of the proposed optimization in Sect. III-C.

which additionally regulates the $0^+0^-$ subspace. This property is crucial, when the demanded speeds and/or the constant power range (i.e. in the FW mode) are as critical as the applied electromagnetic torque, as for EV [12]. Compared to the 1N optimization in [7], the proposed optimization in this paper extends the speed range for the 1N and 2N connections by 16.64% and 25.23%, respectively, when comparing $\omega_{e,max}^{FW}$ to the speed corresponding to the operating point of $m_{e,max}$, which is the maximum operating point obtained in [5]–[7]. It is worth to mention that the maximum achievable speed in the healthy case for the employed ADT-IPMSM is 1.43 p.u.; owing to the distributed winding configuration and high characteristic current (i.e. $d$-axis current required to diminish the PM flux), is approximately 11 times the current $\hat{i}_{s,rated}$ in Table I.

Since the speed is taken into account in the presented study, it is of interest to illustrate the post-fault efficiency maps for both connections. Figs. 7(a)-(b) show the variation of the experimentally-identified efficiency throughout the permissible operating range for both the 1N and 2N connections, respectively. The electrical losses used in calculating the efficiency were limited to the stator copper losses. Core losses were ne-

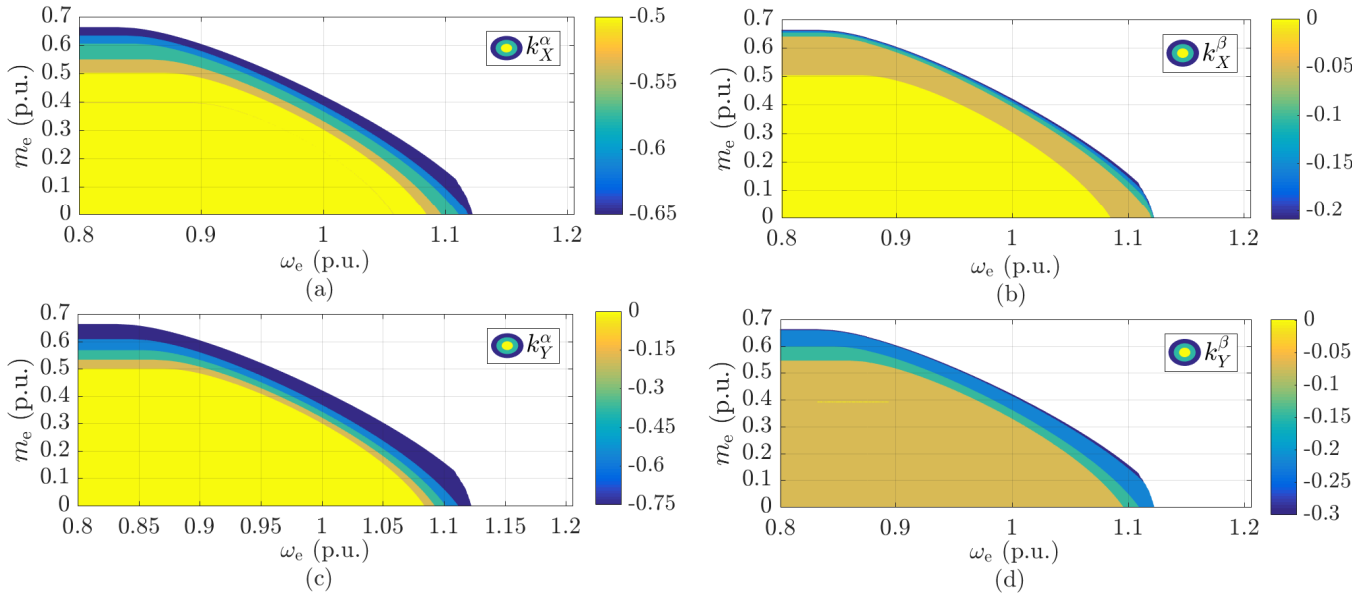


Fig. 8. Post-fault parameters in $\boldsymbol{T}_k$ within the FW region for the 1N connection (see FW region in Fig. 5(a)) computed using the proposed optimization in Sect. III-C: (a) $k_X^\alpha$, (b) $k_X^\beta$, (c) $k_Y^\alpha$, and (d) $k_Y^\beta$.

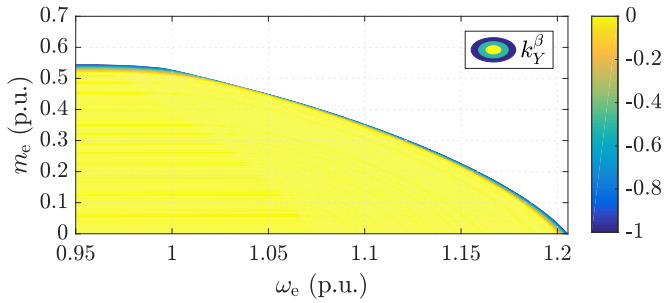


Fig. 9. Post-fault $k_Y^\beta$ within the FW region for the 2N connection (see FW region in Fig. 5(b)) computed using the optimization in Sect. III-C.

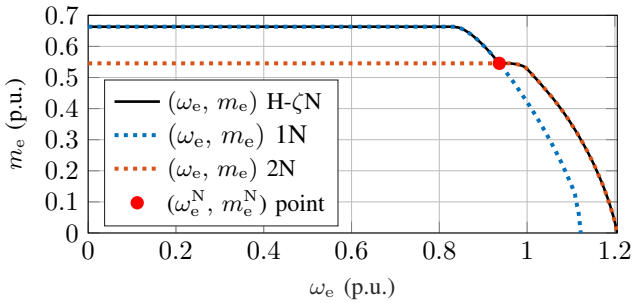


Fig. 10. Post-fault $(m_e, \omega_e)$ characteristics 1N, 2N, and H-ξN connections.

glected since they become significant only at high operational speeds, which is not the case here [19]. It was found out that the difference in efficiency between both connections is minor within the common $(m_e, \omega_e)$ loci. Nevertheless, it was concluded that the 1N connection achieves higher efficiency at low-speed/high-torque regions in comparison with the 2N connection which achieves relatively higher efficiencies at high speeds. Owing to the additional degree of freedom of the 1N connection for a given torque, the optimization selects lower values for the parameters of $\boldsymbol{T}_k$ compared to the 2N connection case. Thus, at low-speed/high-torque operation, the magnitude of the $\boldsymbol{i}_s^{XY}$ and $\boldsymbol{i}_s^0$ currents of the 1N connection are lower than that of $\boldsymbol{i}_s^{XY}$ of the 2N connection.

The corresponding parameters in $\boldsymbol{T}_k$ for both neutral connections in the FW mode are indicated in Figs. 8-9, which represent the necessary variations throughout points to satisfy the constraints in (12). For the 2N case, since $k_X^\alpha = -1$, $k_X^\beta = 0$ (see Sect. III-A), the optimization sets $k_Y^\alpha = 0$ as the optimum value throughout the entire operating range. From real-time implementation point of view, the 2N connection could be favourable owing to the lower memory requirements; as only $k_Y^\beta$ needs to be saved as a look-up-table (LUT) compared to the 1N connection (i.e. $k_X^\alpha$, $k_X^\beta$, and $k_Y^\alpha$ should be additionally stored as well).

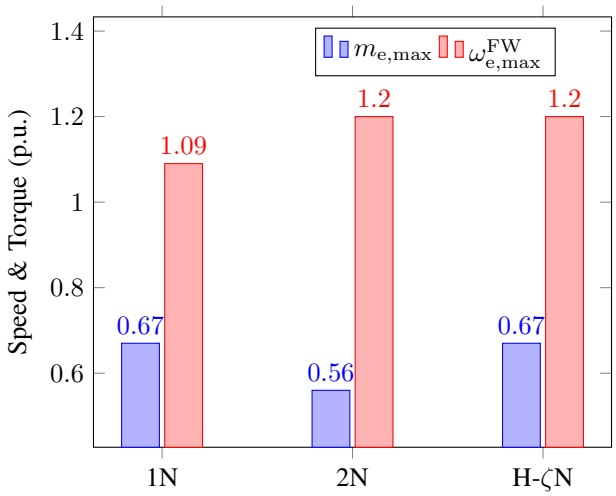


Fig. 11. Post-fault comparison between the exploited torque-speed limits of the proposed H-ζN connection and those achieved by the 1N and 2N connections upon applying the optimization in Sect. III-C.

It is possible to combine the merits of both neutral point connections by installing a neutral point switch altering between 1N or 2N connections (see Fig. 1), leading to a hybrid neutral connection termed H-ξN, where $\xi \in \{1, 2\}$. Accordingly, torque-speed characteristics are shown in Fig.

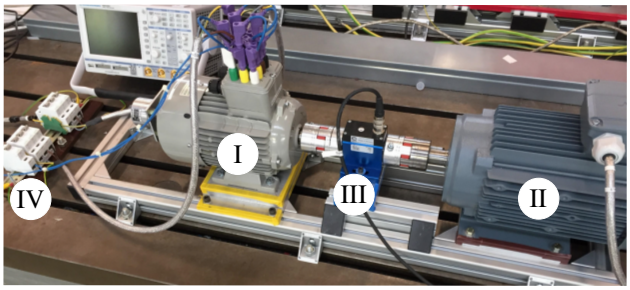


Fig. 12. Test bench: (I) ADT-IPMSM, (II) induction machine (i.e. prime mover), (III) torque sensor, and (IV) stator and neutral points circuit breakers.

10, where both the maximum torque and speed of the 1N and 2N connections are realized. The highlighted operating intersection point "●" $(\omega_{\mathrm{e}}^{\mathrm{N}}, m_{\mathrm{e}}^{\mathrm{N}})$ in Fig. 10 represents the boundary point separating the H-1N and H-2N connections, where the ADT-IPMSM operates in the 1N mode only if $\omega_{\mathrm{e}} < \omega_{\mathrm{e}}^{\mathrm{N}}$ OR $m_{\mathrm{e}} > m_{\mathrm{e}}^{\mathrm{N}}$. Otherwise, the 2N connection is selected. Accordingly, the parameters of $\boldsymbol{T}_k$ are selected as shown in Figs. 8 and 9 depending on the selected neutral point. Further illustrations are shown in the experimental results in Sect. IV. Finally, the maximum limits in terms of torque-speed for 1N, 2N, and H-ξN are illustrated as a bar plot shown in Fig. 11. It is clear that the proposed H-ζN connection combines both merits of 1N and 2N configurations, maximizing the drive's torque and speed capability in the post-fault operation.

## IV. Experimental Results

The proposed post-fault optimization is tested on a torque-controlled 2.5 kW ADT-IPMSM drive, which is coupled to a standard three-phase induction machine operating in motor mode (see Fig. 12). Circuit breakers are installed between the inverters and the stator terminals to disconnect the desired phase (i.e. phase $\mathrm{a}_1$ in this case) as well as the neutral points, modifying the connection as desired. The $\boldsymbol{T}_k$ maps in Figs. 8 and 9 are downloaded as a $21 \times 21$ look-up-table on the real-time dSPACE DS1007 platform. As for the FOC-based current controller, the fundamental harmonic controllers are implemented as shown in Fig. 1, while tuned similar to the controller in [14]; ensuring stable operation through the entire speed range. A sinusoidal carrier-based pulse-width-modulation (PWM) is adopted to dispatch the computed voltages in Fig. 1 by controlling appropriately the inverter switches. Employment of other PWM schemes for instance to reduce common-mode voltages and ground leakage currents has not been considered in this paper for simplicity [20]. In this paper, the current controller structure is as that in [14], with a key difference that the reference currents for the $XY$ and *zero* subspaces are selected according to (7). The resonant controllers are discretized using the impulse invariant method with two samples delay compensation scheme; to ensure stable operation for all resonant controllers within the operating speed range [10]. It is worth to mention that the adopted current controller in [4] is incapable of producing high-quality stator currents; as the authors in [4] employ two mechanically-coupled three phase machines as an approximation for the dual three-phase structure. The fact that the two three-phase sets are magnetically decoupled would diminish the presence of the $XY$ subspace and harmonic currents control could be neglected [4]. The presented line-to-line voltages shown later were computed from the reference phase voltages before being dispatched to the PWM block on dSPACE.

The presented optimization is tested first for the 1N connection shown in Fig. 13, where the torque is set to 0.6 p.u., such that the speed reference is varied in steps, corresponding to points lying on $\Omega_{\mathrm{e}}^{\mathrm{MTPA}}$ and $\Omega_{\mathrm{e}}^{\mathrm{FW}}$ (see Fig. 13(a)). Afterwards, the speed is set to the maximum permissible speed $\omega_{\mathrm{e,max}}^{\mathrm{FW}}$ for the 1N connection, which in return nullifies the generated torque. This is evident by the $i_{\mathrm{s}}^{q}$ current in Fig. 13(b). If the operating point was set to the maximum permissible torque of $\approx 0.67$ p.u., then operating speed points on the loci $\Omega_{\mathrm{e}}^{\mathrm{MTPA}}$ and $\Omega_{\mathrm{e}}^{\mathrm{FW}}$ would be identical. Owing to the employed control structure in Fig. 1, the stator currents tracks the fundamental component while compensating the unwanted harmonics, as seen in the Figs. 13(c)-(d). On the other hand, the most significant line-to-line voltages of $\bar{\boldsymbol{u}}_{\mathrm{s,1N}}^{l\text{-}l}$ (i.e. voltages approaching 1 p.u.) in (10), are observed in Fig. 13(e), with its zoomed plots in Figs. 13(f)-(h). For different time intervals, depending on the $m_{\mathrm{e}}$ and $\omega_{\mathrm{e}}$ variations, the parameters of $\boldsymbol{T}_k$ manipulate the subspace currents to keep the voltages within 1p.u. (i.e. satisfying $g_5$ for the 1N case) as well as satisfying $g_4$, validating the proposed post-fault optimization for the 1N connection. It should be noted that the line-to-line voltage distortions increase with speed (see Figs. 13(g)-(h)), owing to the increased harmonic content in the stator currents which subsequently increases the harmonic controllers control action in Fig. 1, to force sinusoidal $\boldsymbol{i}_{\mathrm{s}}^{a_1 \rightarrow c_2}$ currents through the stator terminals [14]. On the other hand, a similar test has been carried-out for the 2N neutral configuration, where a lower torque reference 0.4 p.u. has been set; since a torque reference 0.6 p.u. in that case would violate $g_4$ (see Fig. 5(b)). To achieve the maximum possible speed $\omega_{\mathrm{e,max}}^{\mathrm{FW}}$ for the 2N case, the maximum current vector was set in the $d$ current direction, as seen in Fig. 14(b). The stator line-to-line voltages in that case are shown in Fig. 14(e), with its zoomed versions in Figs. 14(f)-(h). When the machine is brought to its maximum speed limit, the voltages distortions increase, as seen in Fig. 14(h), to inject sinusoidal stator currents shown in Fig. 14(d). Owing to the RC action at $\omega_{\mathrm{e,max}}^{\mathrm{FW}}$, the $\bar{\boldsymbol{u}}_{\mathrm{s,2N}}^{l\text{-}l}$ in Fig. 14(h) tend to exceed the 1 p.u. range, yet in a limited range (i.e. 1.04 p.u.), which is mitigated by raising the PWM voltage limit through the DC-link voltage $u_{\mathrm{dc}}$ by only 4%. However, the voltage reserve in the available tests is fixed and already high enough 580 V compared to the rated voltage $\hat{u}_{\mathrm{s,rated}}^{l\text{-}l}$ as seen in Table I. It is worth to mention that even if a high percentage overvoltage is allowed (at least for low voltage motors), a significant imminent danger is not overseen; since the winding insulation is usually designed to withstand much higher voltages than the rated one. However, overvoltage operations tend to increase the leakage current to ground point through the bearings, which in turn decrease their average lifetime (i.e. operating hours) [21].

Next, the merits of both 1N and 2N connections are realized by the proposed H-ζN connection, which is tested experimentally in Figs. 15(a)-(b). The speed ramps up from

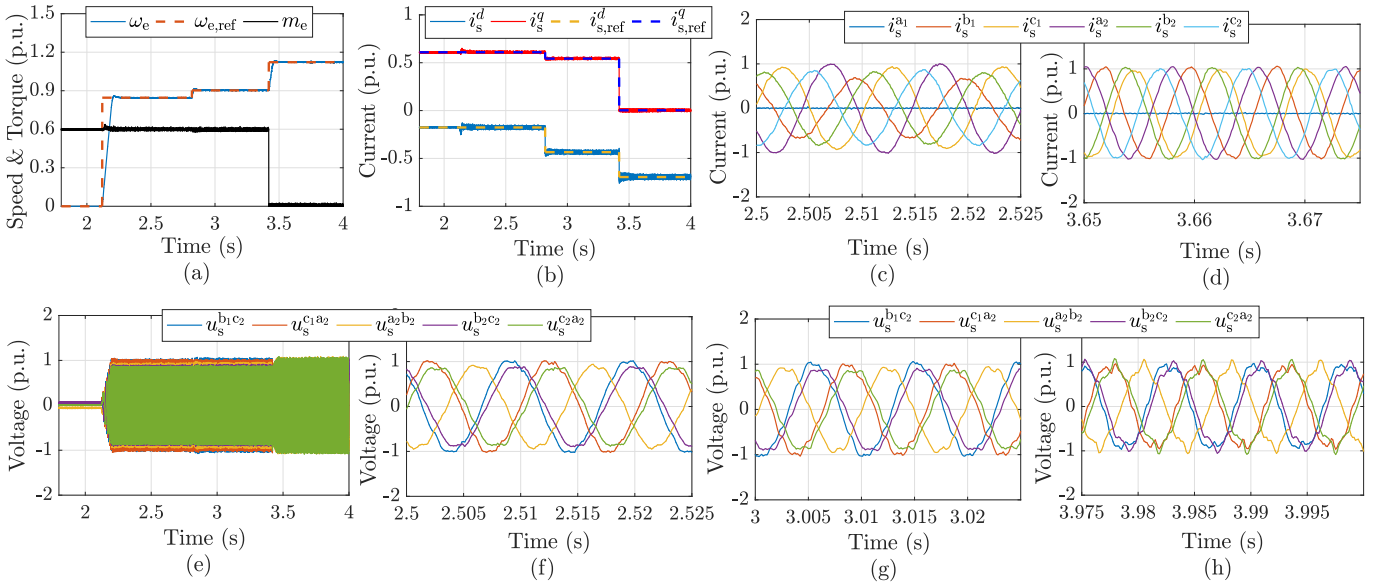


Fig. 13. Post-fault operation results of the proposed optimization for the 1N connection: (a) speed and torque, (b) $dq$ currents, (c)-(d) stator currents at $\Omega_{\mathrm{e}}^{\mathrm{MTPA}}$ and maximum $\Omega_{\mathrm{e}}^{\mathrm{FW}}$, the corresponding significant line-to-line voltages in (e) along with the zoomed versions in (f)-(h).

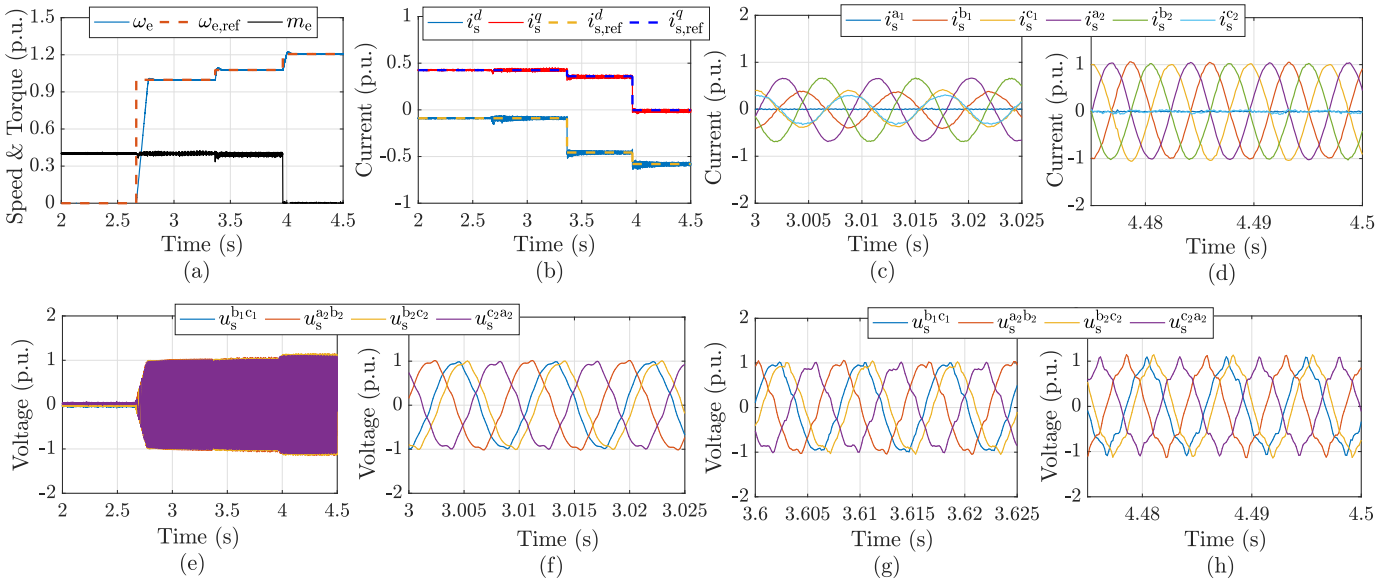


Fig. 14. Post-fault operation results of the proposed optimization for the 2N connection: (a) speed and torque, (b) $dq$ currents, (c)-(d) stator currents at $\Omega_{\mathrm{e}}^{\mathrm{MTPA}}$ and maximum $\Omega_{\mathrm{e}}^{\mathrm{FW}}$, the corresponding line-to-line voltages in (e) along with the zoomed versions in (f)-(h).

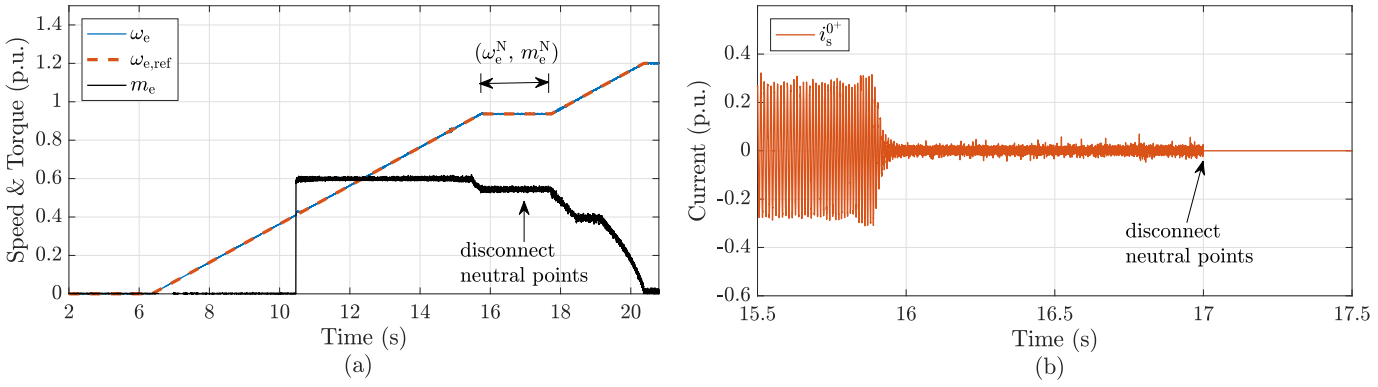


Fig. 15. Post-fault H-ζN operation showing (a) the torque-speed profile highlighting the $(\omega_{\mathrm{e}}^{\mathrm{N}}, m_{\mathrm{e}}^{\mathrm{N}})$ points and the instant of disconnecting the neutral points, which is evident in (b) showing $i_{\mathrm{s}}^{0^+}$ before and after disconnection according to the explained sequence in Sect. IV.

standstill to the $\omega_{\mathrm{e,max}}^{\mathrm{FW}}$ of the 2N case (i.e. $\omega_{\mathrm{e,max}}^{\mathrm{FW}} = 1.2$ p.u.), while the applied torque combines those operating points of 1N and 2N modes in Fig. 13(a) and Fig. 14(a) (i.e. 0.6 and 0.4 p.u.), as seen in Fig. 15(a). The neutral point breaker should be switched ON/OFF depending on the location of the operating point in Fig. 10 with respect to $(\omega_{\mathrm{e}}^{\mathrm{N}}, m_{\mathrm{e}}^{\mathrm{N}})$ point, as explained in Sect. III-D and in Fig. 10. When the neutral point connection is set to H-2N, then the *zero* frame controller in Fig. 1 is deactivated and vice-versa for the H-1N case. Practically, to avoid switching in the presence of neutral currents when changing from H-1N to H-2N connection, the controller first switches to the parameters in $\boldsymbol{T}_k$ of the 2N connection; sets $\boldsymbol{i}_{\mathrm{s,ref}}^{0} = 0$; then the neutral switch state is toggled; and finally the *zero* sequence controller is deactivated (see Fig. 15(b)). Indeed, improved practical neutral points toggling schemes could be studied, such as faster toggling scheme and/or introducing hysteresis band to avoid chattering if the operating point is located near $(\omega_{\mathrm{e}}^{\mathrm{N}}, m_{\mathrm{e}}^{\mathrm{N}})$. However, such toggling strategies will be considered in future work. This paper focuses on illustrating the philosophy of neutral point switching and its effect on both torque and speed. Since the neutral point controls the flow of only $\boldsymbol{i}_{\mathrm{s}}^{0}$, it is expected that toggling the neutral point status would not affect the electromechanical torque, as shown in Fig. 15(a).

## V. Conclusion

This paper presented a modified offline optimization scheme, capable of identifying the optimization parameters throughout the entire torque-speed range and for different neutral point configurations, unlike literature which only considered fault-tolerance from the electromechanical torque point of view for the 1N connection. The computed optimization parameters were put under study for different operating regimes (i.e. MTPA or FW), where the practical results adhered to the drawn out expectations. The merits of both 1N and 2N configurations, in terms of higher torque production and maximum speed, respectively, have been combined together within the proposed H-$\zeta$N connection. Through the applied torque-speed profile, the operation in the H-1N, H-2N and transition between both connections has been illustrated, verifying the laid-out assumptions. Although the speed enhancement cannot be quantifiably generalized to all ADT-IPMSM drives, owing to parameter dependency, the obtained findings are of interest when both the maximum achievable speed and torque during post-fault operation are crucial. Future work will target investigating PM machine designs, especially with extended constant-power speed range, to draw broader conclusions. The verification has been carried-out practically on a 2.5 kW ADT-IPMSM, confirming the effectiveness of the proposed optimization scheme.

## Acknowledgment

This work is supported by the project AWESCO (H2020-ITN-642682) funded by the European Union's Horizon 2020 research and innovation program under the Marie Sklodowska-Curie grant agreement No. 642682.

## References

[1] E. Levi, "Multiphase electric machines for variable-speed applications," *IEEE Trans. on Ind. Electron.*, vol. 55, pp. 1893–1909, May 2008.

[2] R. Bojoi, M. Lazzari, F. Profumo, and A. Tenconi, "Digital field-oriented control for dual three-phase induction motor drives," *IEEE Trans. on Ind. Appl.*, vol. 39, pp. 752–760, May 2003.

[3] A. S. Abdel-Khalik, S. Ahmed, and A. M. Massoud, "A nine-phase six-terminal concentrated single-layer winding layout for high-power medium-voltage induction machines," *IEEE Trans. on Ind. Electron.*, vol. 64, pp. 1796–1806, March 2017.

[4] W. Wang, J. Zhang, M. Cheng, and S. Li, "Fault-tolerant control of dual three-phase permanent-magnet synchronous machine drives under open-phase faults," *IEEE Trans. on Power Electron.*, vol. 32, pp. 2052–2063, March 2017.

[5] H. S. Che, M. J. Duran, E. Levi, M. Jones, W. P. Hew, and N. A. Rahim, "Postfault operation of an asymmetrical six-phase induction machine with single and two isolated neutral points," *IEEE Trans. on Power Electron.*, vol. 29, pp. 5406–5416, Oct 2014.

[6] W. N. W. A. Munim, M. Duran, H. S. Che, M. Bermudez, I. Gonzalez-Prieto, and N. A. Rahim, "A unified analysis of the fault tolerance capability in six-phase induction motor drive," *IEEE Trans. on Power Electron.*, vol. 32, no. 10, pp. 7824–7836, 2016.

[7] F. Baneira, J. Doval-Gandoy, A. G. Yepes, . López, and D. Pérez-Estévez, "Control strategy for multiphase drives with minimum losses in the full torque operation range under single open-phase fault," *IEEE Trans. on Power Electron.*, vol. 32, pp. 6275–6285, Aug 2017.

[8] I. Gonzalez-Prieto, M. J. Duran, H. S. Che, E. Levi, M. Bermúdez, and F. Barrero, "Fault-tolerant operation of six-phase energy conversion systems with parallel machine-side converters," *IEEE Trans. on Power Electron.*, vol. 31, pp. 3068–3079, April 2016.

[9] E. Levi, D. Dujic, M. Jones, and G. Grandi, "Analytical determination of dc-bus utilization limits in multiphase vsi supplied ac drives," *IEEE Trans. on Energy Conversion*, vol. 23, pp. 433–443, June 2008.

[10] A. G. Yepes, J. Doval-Gandoy, F. Baneira, D. Perez-Estevez, and O. Lopez, "Current harmonic compensation for $n$ -phase machines with asymmetrical winding arrangement and different neutral configurations," *IEEE Trans. on Ind. Appl.*, vol. 53, pp. 5426–5439, Nov 2017.

[11] J. Lemmens, P. Vanassche, and J. Driesen, "Optimal control of traction motor drives under electrothermal constraints," *IEEE Journal of Emerging and Selected Topics in Power Electronics*, vol. 2, pp. 249–263, June 2014.

[12] E. Trancho, E. Ibarra, A. Arias, I. Kortabarria, J. Jurgens, L. Marengo, A. Fricassè, and J. V. Gragger, "PM-assisted synchronous reluctance machine flux weakening control for ev and hev applications," *IEEE Trans. on Ind. Electron.*, vol. 65, pp. 2986–2995, April 2018.

[13] M. Tousizadeh, H. S. Che, N. A. Rahim, J. Selvaraj, and B. T. Ooi, "Performance comparison of fault-tolerant three-phase induction motor drives considering current and voltage limits," *IEEE Trans. on Ind. Electron.*, 2018 (doi:10.1109/TIE.2018.2850006).

[14] H. M. Eldeeb, A. S. Abdel-Khalik, and C. M. Hackl, "Dynamic modeling of dual three-phase ipmsm drives with different neutral configurations," *IEEE Trans. on Ind. Electron.*, vol. 66, pp. 141–151, Jan 2019.

[15] C. M. Hackl, *Non-identifier based adaptive control in mechatronics: Theory and Application*. No. 466 in Lecture Notes in Control and Information Sciences, Berlin: Springer International Publishing, 2017.

[16] C. M. Hackl, M. J. Kamper, J. Kullick, and J. Mitchell, "Current control of reluctance synchronous machines with online adjustment of the controller parameters," in *in Proceedings of the 2016 IEEE International Symposium on Ind. Electron. (ISIE 2016)*, (Santa Clara, CA, USA), pp. 156–160, 2016.

[17] M. J. Duran, I. Gonzalez-Prieto, N. Rios-Garcia, and F. Barrero, "A simple, fast, and robust open-phase fault detection technique for six-phase induction motor drives," *IEEE Trans. on Power Electron.*, vol. 33, pp. 547–557, Jan 2018.

[18] A. G. Yepes, J. Doval-Gandoy, F. Baneira, and H. Toliyat, "Control strategy for dual three-phase machines with two open phases providing minimum loss in the full torque operation range," *IEEE Trans. on Power Electron.*, 2018 (doi:10.1109/TPEL.2018.2830507).

[19] J. Kim, I. Jeong, K. Nam, J. Yang, and T. Hwang, "Sensorless control of PMSM in a high-speed region considering iron loss," *IEEE Trans. on Ind. Electron.*, vol. 62, pp. 6151–6159, Oct 2015.

[20] Z. Liu, Z. Zheng, S. D. Sudhoff, C. Gu, and Y. Li, "Reduction of common-mode voltage in multiphase two-level inverters using spwm with phase-shifted carriers," *IEEE Trans. on Power Electron.*, vol. 31, pp. 6631–6645, Sept 2016.

[21] J. M. Erdman, R. J. Kerkman, D. W. Schlegel, and G. L. Skibinski, "Effect of pwm inverters on ac motor bearing currents and shaft voltages," *IEEE Trans. on Ind. Appl.*, vol. 32, pp. 250–259, Mar 1996.

**Hisham M. Eldeeb** received his B.Sc. (honors) and M.Sc. in electrical engineering in 2011, 2014, respectively, from the Faculty of Engineering, Alexandria University, Egypt. From 2012 to 2015, he worked as a research associate at the College of Engineering, Qatar University in Qatar, where he was hired on 1.4M$ project; aiming at extending the amount of penetration of inverter-based distributed-generation plants within the Qatari-Network. From September 2015, he was selected as one of the 14 Marie-Curie Ph.D. candidates hired on the 3M€ EU Horizon H2020 project "Airborne Wind Energy System Control and Optimization" (AWESCO). He is currently working as a research associate at the Munich University of Applied Sciences (MUAS) and pursuing his Ph.D. degree at the Technical University of Munich (TUM), Germany. His research interests are grid-connected converters, power quality issues, power electronics, electrical drives, and optimal control.

**Ayman S. Abdel-Khalik** (SM'12) received the B.Sc. and M.Sc. degrees in electrical engineering from Alexandria University, Alexandria, Egypt, in 2001 and 2004, respectively, and the Ph.D. degree in electrical engineering from Alexandria University, and Strathclyde University, Glasgow, U.K., in 2009, under a dual channel program. He is currently an Associate Professor with the Electrical Engineering Department, Faculty of Engineering, Alexandria University, Alexandria, Egypt. He serves as an Associate Editor of IET Electric Power Applications Journal and the Executive Editor of Alexandria Engineering Journal. His current research interests include electrical machine design and modelling, electric drives, energy conversion, and renewable energy.

**Christoph M. Hackl** (M'12 - SM'16) was born in 1977 in Mannheim, Germany. After studying electrical engineering (controls and mechatronics) at Technical University of Munich (TUM), Germany and University of Wisconsin-Madison, USA, he received the B.Sc., Dipl.-Ing., and Dr.-Ing. (Ph.D.) degree in 2003, 2004 and 2012 from TUM, respectively. Since 2004, he is teaching electrical drives, power electronics, and mechatronic & renewable energy systems. Since 2014, he is heading the research group "Control of Renewable Energy Systems (CRES)" at TUM. In 2018, he was appointed Professor for Electrical Machines and Drives and heads the "Laboratory for Mechatronic and Renewable Energy Systems (LMRES)" at the Munich University of Applied Sciences (MUAS), Germany. His main research interests are nonlinear, adaptive and optimal control of electric, mechatronic and renewable energy systems.